

OPEN ACCESS

Fast Charging of Li-Ion Cells: Part II. Nonlinear Contributions to Cell and Electrode Polarization

To cite this article: Ilya A. Shkrob *et al* 2019 *J. Electrochem. Soc.* **166** A3305

View the [article online](#) for updates and enhancements.

You may also like

- [Measurement of Ionic Conductivity and Electrode Polarization at Low Temperatures on 8YSZ by a DC Technique](#)
Alexander Szendrei, Taylor D. Sparks and Anil V. Virkar
- [Influence of the Complex Interface between Transport and Catalyst Layer on Water Electrolysis Performance](#)
Tien-Ching Ma, Andreas Hutzler, Boris Bensmann *et al.*
- [Electrode polarization in dielectric measurements: a review](#)
Paul Ben Ishai, Mark S Talary, Andreas Caduff *et al.*



Your Lab in a Box!

The PAT-Tester-i-16: All you need for Battery Material Testing.

- ✓ All-in-One Solution with integrated Temperature Chamber!
- ✓ Cableless Connection for Battery Test Cells!
- ✓ Fully featured Multichannel Potentiostat / Galvanostat / EIS!

www.el-cell.com +49 40 79012-734 sales@el-cell.com

EL-CELL[®]
electrochemical test equipment





Fast Charging of Li-Ion Cells: Part II. Nonlinear Contributions to Cell and Electrode Polarization

Ilya A. Shkrob,^{1b} Marco-Tulio Fonseca Rodrigues,^{1b} Dennis W. Dees,^{1b} and Daniel P. Abraham^{1b,*},^z

Chemical Sciences and Engineering Division, Argonne National Laboratory, Lemont, Illinois 60439, USA

In this series, Li/Cu microprobes are used to monitor potentials of individual electrodes in situ during high-rate charging of Li-ion cells. Here we focus on capacity-limited charging of these cells to 6C, and present a general treatment of polarization that allows for data reduction and accurate interpolation/extrapolation over a wide range of charge rates. We show that the anode impedance as measured both using this new treatment and the more established pulsed-current techniques is not significantly changed after high-rate aging of the cell, including the conditions under which Li plating has occurred. Our measurements suggest that the changes in cell and electrode polarization to a large extent occur through nonlinear effects that involve time-delayed processes. An electrochemical model that includes phase dynamics in lithiated graphite is shown to capture some but not all of the observed trends suggesting that important facets of the high-rate behavior need to be included in such models.

© The Author(s) 2019. Published by ECS. This is an open access article distributed under the terms of the Creative Commons Attribution 4.0 License (CC BY, <http://creativecommons.org/licenses/by/4.0/>), which permits unrestricted reuse of the work in any medium, provided the original work is properly cited. [DOI: 10.1149/2.0561914jes]



Manuscript submitted August 16, 2019; revised manuscript received September 11, 2019. Published September 30, 2019.

This article continues a series of studies on fast charging of lithium-ion cells containing a graphite anode and layered oxide cathode. We address the reader to Part I for motivation and objectives of this series.¹ Briefly, increasing the charging rate of Li-ion batteries in electric vehicles above a 1C rate (where 1C corresponds to full discharge in 1 h) is hindered by insufficient understanding of nonequilibrium dynamic processes occurring in the battery cells at the high rates, both on the short and long time scales (see Refs. 2 and 3 for examples of such processes).⁴ In particular, excessive voltage polarization in these regimes leads to conditions favoring Li metal deposition on the graphite that affects both life and safety of the cell.⁵⁻⁷

To assist diagnostic studies, in Part I we introduced microprobe Li/Cu reference electrodes (REs) and used them to characterize the cell during voltage-limited charging.¹ In this mode, constant current charging is terminated when the cell voltage U reaches a set upper cutoff voltage U_{max} (UCV). With this method, the cell can withstand multiple cycles at high currents without significant loss of capacity; however, the terminal state-of-charge (SOC) reached at U_{max} progressively decreases with increasing C-rate due to strong polarization in the cell.¹ Alternatively, the cell can be charged in a capacity-limited mode, in which the electrode and cell potentials are allowed to float with no upper bound. The advantage of capacity-limited charging over voltage-limited charging is that it permits the study of *high-currents in higher SOC regimes*, which can reveal behaviors that also occur under milder charging conditions, but may be less obvious.

In particular, cell and electrode polarization become pronounced at high C-rates as the cell is charged (Figure 1 showing a typical example). This polarization originates through resistance to charge current and kinetic delays in the electrodes, and it causes the cell voltage $U = \phi_c - \phi_a$ and the cathode potential ϕ_c to increase, and the anode potential ϕ_a to decrease, with the increasing current I . Excessive cathode polarization is a concern as it can result in electrolyte oxidation and cause permanent structural changes in the layered oxide. Excessive anode polarization almost guarantees that in some charging regimes the electrode surface potential will become negative, and Li plating will occur due to proximity of the lithiated graphite potential vs. metallic Li (~ 85 mV vs. Li/Li⁺).^{5,8}

In this study, we introduce a general methodology to characterize cell and electrode polarization that occurs during charging at high rates. This new method complements the more established impedance measurement techniques, such as the hybrid pulse power characterization (HPPC) and a. c. electrochemical impedance spectroscopy (EIS).⁹⁻¹¹ An important limitation of these conventional techniques

is that they mainly quantify fast ($< 10^2$ s) linear responses to changing currents.¹⁴ Here we demonstrate that nonlinear changes occurring on a longer time scale are equally important, and at high rates these contributions can be responsible for a large fraction of the observed polarization. For the graphite electrode, this nonlinear contribution is entirely responsible for changes observed during high-rate aging of the cells. To assess whether electrochemical models can describe this nonlinearity, a state-of-the-art Newman-style model that includes phase dynamics in the lithiated graphite electrode¹² was used to simulate the experimental results. While some of these observations can be

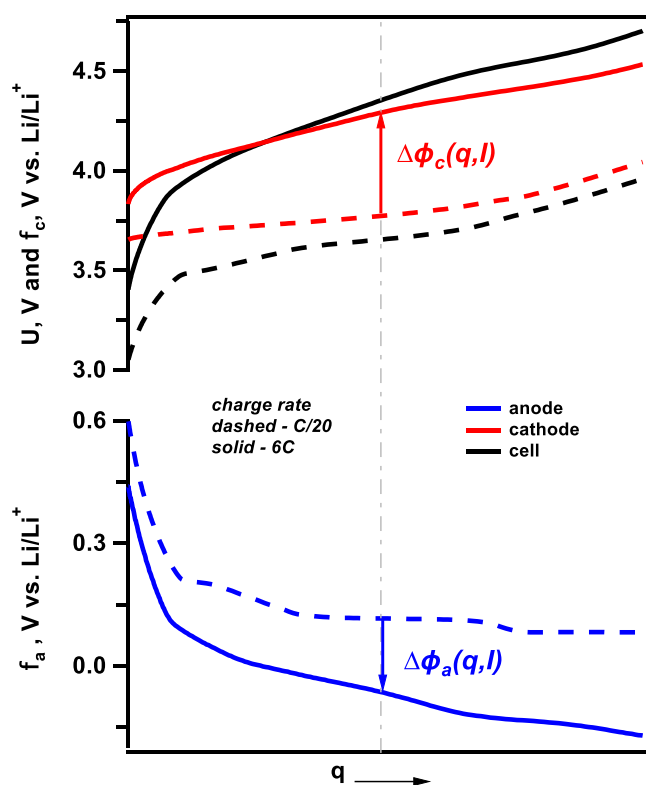


Figure 1. Typical $V(q,I)$ curves (full-cell and electrode potentials) obtained during slow (C/20, dashed lines) and fast (6C, solid lines) charging. The difference between these curves for a fixed charge q represents polarization in the cell (the color arrows).

*Electrochemical Society Member.

^zE-mail: abraham@anl.gov

qualitatively reproduced, it is seen that other behaviors would require further development of such models.¹³

In addition to the table and figures in the main text, supplementary data are included in the Supporting Information (SI). When referenced in the main text, these materials have the designator “S”, as in Figure S1. The SI also gives the full list of abbreviations used in the text.

$r_{1,2}$ Methodology

Formally, the electrode and/or cell potentials V are continuous functions of charge $q(t) = It$ transferred by the constant current I over the time period t (Figure 1). This charge q equals cell capacity and/or state of charge (SOC) in the appropriate units. In a typical experiment, a family of $V(q, j)$ plots is obtained for different current densities j . Let us define $V(q, 0)$ as the potential for an infinitely small current so that

$$\Delta V(q, j) = V(q, j) - V(q, 0). \quad [1]$$

For small currents, $V(q, j)$ can be expanded in a Taylor series; by retaining only linear and quadratic terms, one obtains

$$\Delta V(q, j) \approx j r_1(q) + j^2 b(q) + O(j^3). \quad [2]$$

In this expression, $r_1(q)$ and $b(q)$ are the functions of capacity q , but not the current. Dropping the terms in the parentheses, for such small currents Eq. 2 can be recast as

$$\Delta V(q, j) \approx j r_1 \{1 + jb/r_1\} \approx j r_1 / \{1 - jb/r_1\} \quad [3]$$

Introducing the new parameter $r_2 = b/r_1$, from Eq. 3 we obtain

$$\Delta V(q, j) \approx j r_1 / (1 - j r_2) \quad [4a]$$

that would be valid for small currents only. As shown below, Eq. 4a is also surprisingly accurate at higher currents; that is, $V(q, j)$ can be expressed as

$$V(q, j) \approx V(q, 0) + j r_1 / (1 - j r_2) \quad [4b]$$

even for currents beyond the expected range of validity for Eq. 2. This equation was discovered by us through trial and error using multiple data sets obtained for multiple cells; at this time we cannot provide the rationale why this empirical equation fits the experimental data so well.

Note that the r_1 parameter has the units of area specific impedance (ASI, $\Omega \cdot \text{cm}^2$) while the r_2 parameter has the units of reciprocal current density (cm^2/A). The linear term r_1 in Eq. 4 (which is negative for the anode in our convention) can be compared to the ASI measured using pulsed current techniques. In such measurements, short (2-30 s) current pulses are forced through the cell, and potential difference at the beginning and end of the pulse is used to estimate the impedance for each electrode. However, at high C-rates even short pulses can transfer significant charge, so (unlike r_1 in Eq. 4) the ASI does not correspond to a fixed q . Furthermore, as we show in Part 3 of this series,¹⁴ some components of the time response are spread over several decades in time, and different techniques for evaluating the impedance can yield different estimates.

The functional form of Eq. 4 results in nonlinear dependencies for various quantities of interest, such as potentials and states of charge

corresponding to the onset of a given condition. The chief attraction of this equation is that it allows considerable data reduction and extrapolation from a limited set of experiments. In the following, we will use Eq. 4 to better characterize the behaviors observed during capacity-limited charging of a full cell, which includes its aging behavior.

Experimental

Materials.—Electrochemical experiments described in this section were conducted using electrodes fabricated at Argonne National Laboratory’s Cell Analysis, Modeling, and Prototyping (CAMP) Facility. A $\text{Li}_{1.03}(\text{Ni}_{0.5}\text{Co}_{0.2}\text{Mn}_{0.3})_{0.97}\text{O}_2$ (NCM523) cathode and graphite anode were used in all cells. Table I details the composition and characteristics of the electrodes. Carbon particles (C45, Timcal) were used to provide electronic conductivity in the matrix and polyvinylidene fluoride (PVdF) was used as a binder. The electrodes were dried in a vacuum oven set at 120°C before cell assembly. The electrolyte consisted of 3:7 w/w mixture of ethylene carbonate and ethyl methyl carbonate with 1.2 M lithium hexafluorophosphate (LiPF_6). Details of the reference electrode (RE) preparation and electrochemical cell assembly are described in previous articles.^{1,15} Briefly, the RE probe consisted of a copper wire (25 μm diameter) with a thin layer of Li metal plated on the exposed tip (2 mm). The probe was positioned between (and at the center of) two microporous separators (Celgard 2320) that were sandwiched between the 20.3 cm^2 area electrodes. Cell assembly and testing were conducted inside an Ar-atmosphere glove box.

Galvanostatic tests.—All tests were conducted at 30°C using a Maccor Model 2400 battery cycler. Formation cycling included two C/10 cycles, followed by one C/25 cycle, between 3–4.1 V. A rate of 1C corresponds to 40 mA, and a nominal capacity of 120 $\text{mAh/g}_{\text{oxide}}$ was used as 100% SOC (which corresponds to an area specific capacity of $\sim 2 \text{ mAh/cm}^2$). Note that all specific capacities stated in this manuscript are normalized by weight of the oxide material in the cathode. The test protocol involved charging the cell to a set capacity (or SOC) using a constant current followed by a ~ 2 h rest at open circuit. After the rest, the cell was discharged to the lower cutoff voltage (LCV) set to 3 V at a relatively slow C/5 rate. This step was followed by a potentiostatic hold at 3 V to enable reinsertion of the cyclable lithium into the cathode. In each series, the charge C-rate progressively increased with each cycle from 0.05 to 6 (this is referred to as C-rate escalation). This protocol ensures that cell damage (if any) occurring at high rates does not compromise the lower rate measurements.

Aging tests.—To characterize aging of the cell, a {0.5, 1, 2, 3, 4, 5, 6} C-rate escalation followed by C/5 discharge was repeated eight times with the maximum capacity set to 50 $\text{mAh/g}_{\text{oxide}}$ ($\sim 0.84 \text{ mAh/cm}^2$). When the capacity was set to 120 $\text{mAh/g}_{\text{oxide}}$, the cell performance degraded rapidly during repeated cycling, disallowing quantitative measurements. Each escalation lap was followed by pulsed-current impedance measurements conducted as described below.

Table I. Cell materials and electrode characteristics.

Positive Electrode (20.3 cm^2 area)	Negative Electrode (20.3 cm^2 area)
90 wt% NCM523 (Toda America)	91.8 wt% Superior Graphite (SLC1506T)
5 wt% C45 (Timcal)	2 wt% C45 (Timcal) + 0.2 wt% oxalic acid
5 wt% PVdF binder (Solvay 5130)	6 wt% PVdF binder (KF-9300 Kureha)
18.6 mg/cm^2 loading density - coating	9.9 mg/cm^2 loading density - coating
16.8 mg/cm^2 loading density - active/oxide	9.1 mg/cm^2 loading density - active/graphite
35.4% electrode porosity	34.5% electrode porosity
71- μm -thick composite coating	70- μm -thick composite coating
20- μm -thick Al current collector	10- μm -thick Cu current collector
Separators: 2x Celgard 2320	Electrolyte: 1.2M LiPF_6 in 3:7 w/w ethylene carbonate: ethyl methyl carbonate (Tomiya)

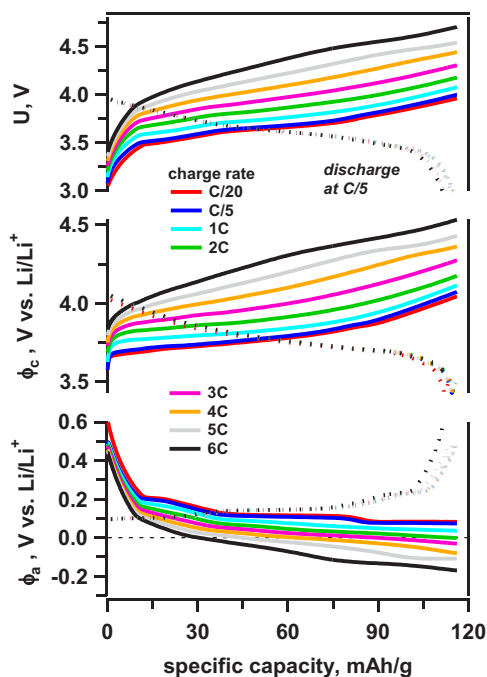


Figure 2. Capacity-limited cycling profiles showing (from top to bottom) the cell voltage, cathode, and anode potentials during charge (solid lines) and discharge (dashed lines). The C/5 discharge capacity showed a noticeable decrease (4.5%) only after the 6C charge.

Pulsed-current measurements.—As the cell resistance/impedance continuously changes during charge, a modified HPPC test was used before and after the high rate charging tests to track these impedance changes. In these experiments, a time response $V(t)$ of the potential to a short ($\tau = 10\text{--}30$ s) rectangular pulse of 3C current is measured at different states-of-charge (or voltages). Before the test, the cell is fully charged at a C/10 rate and then slowly discharged at a C/10 rate to a set SOC (or voltage). A current pulse is applied and followed by 2 min rest, and then another pulse of the same duration but opposite polarity is applied and followed by another 1 h rest (Figure S1). This pulse sequence was repeated for a sequence of preselected cell voltages. As the current is forced through the cell, there is an ohmic component responsible for rapid initial voltage change (< 0.1 s), which is followed by a slower, nearly exponential voltage change with a time constant of tens of seconds. This time-dependent change includes various capacitive and faradaic responses. As it evolves over time, the end-of-pulse “impedance” (defined as $\Delta V(t = \tau)/I$) is also time-dependent. This impedance can be normalized by the electrode area to give the instantaneous ($t = 0$) and end-of-pulse ($t = \tau$) ASI; the time dependent part of ASI (designated as ΔASI) corresponds to the difference between these two quantities.

Results and Discussion

Capacity-limited cycling and data analysis.—Figure 2 shows the cell voltage and electrode potential profiles obtained during capacity-limited charging of the cell at different charge C-rates. In this experiment, the capacity-limit was set to $116 \text{ mAh/g}_{\text{oxide}}$, and was the same for all C-rates. Cell and electrode polarization becomes evident as the charge rate increases beyond 1C. At 6C rate, the cell voltage and cathode potential increase to 4.704 and 4.534 V respectively, while ϕ_a reaches -0.170 V vs. Li/Li^+ . During the ~ 2 h rest at open circuit following the charge step, the cell voltage and electrode potentials gradually relax and become nearly constant after ~ 30 min. Thus, during cell discharge the U , ϕ_c and ϕ_a values start at ~ 3.970 , 4.07 and 0.087 V vs. Li/Li^+ regardless of the rate during the preceding charge

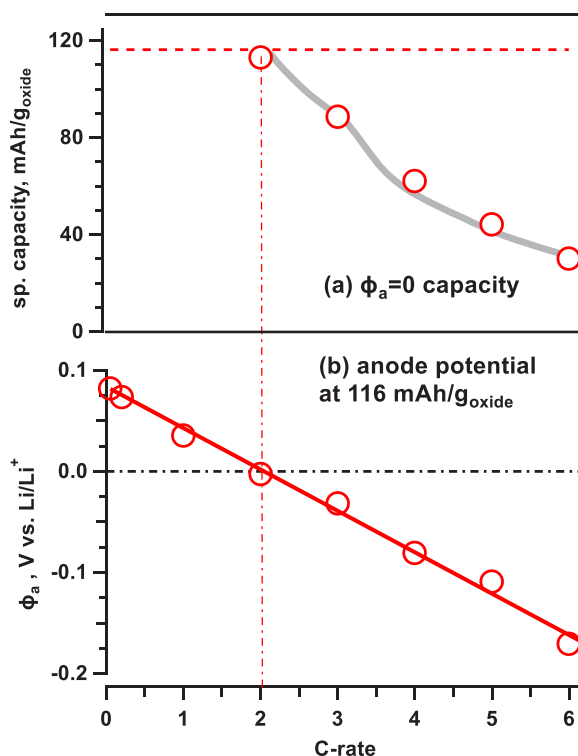


Figure 3. (a) Specific capacity at $\phi_a = 0$ (open circles) and (b) the terminal anode potential during charge and plotted against the C-rates. The gray line in panel (a) is obtained by extrapolating data using the $r_{1,2}$ parameters in Eq. 4. The horizontal red line in panel (a) represents the terminal capacity, and the vertical dash-dot line indicates the zero-crossing current of 2C.

(due to the constancy of the terminal capacity in this experiment). As the current increases, the anode potential crosses zero vs. Li/Li^+ , which would correspond to the onset of Li-plating condition if one neglects resistance between the RE and the electrode surface, as discussed in Part 1 of this series.^{1,5} The zero-crossing ($\phi_a = 0$) capacity systematically decreases with the C-rate and the terminal anode potential at the set capacity decreases linearly with the current (Figures 3a and 3b). Remarkably, for each charging rate at which the anode potential ϕ_a becomes negative at some section of the cycle, the zero crossing of this potential occurs approximately at the same cell voltage, as illustrated in Figures 4a and 4b.

Figure 5 shows fits of the data in Figure 2 using Eq. 4b. The plots are cross cuts of the $V(q, I)$ surface at constant charge q (Figure 1) corresponding to 60% and 96% SOC. A larger family of such curves is shown in Figures S2 and S3; as seen from these plots, the accuracy of Eq. 4 remains good for all conditions provided that the charge $> 3\%$ SOC. Figure 6 shows parameters r_1 and r_2 plotted vs. specific capacity of the cell. It is seen that the cathode makes the larger contribution to r_1 ; for the latter, the higher r_1 for capacities $< 20 \text{ mAh/g}_{\text{oxide}}$ reflects the increased resistance of the oxide particles as they become saturated with lithium.⁵ For all three potentials, r_2 changes sign (at 21% SOC for the cathode and 42% SOC for the anode), so the current dependencies in Eq. 4 transition from sublinear to superlinear during charging of the cell. This nonlinearity causes 20–30% greater potential differences compared to the values linearly extrapolated from low-current regimes.

In Figure 7a, the linear parameter r_1 is plotted as a function of $U(q, 0)$. This parameter is analogous to the ohmic resistance experienced by the electrodes at various charge states and can be compared with the pulsed-current impedance measurements presented later. In Figure 7b, the anode parameters $r_{1,2}$ is plotted vs. $\phi_a(q, 0)$. A $d\phi_a/dq$ plot is also shown to illustrate that the features seen at 0.11 V and 0.20 V vs. Li/Li^+ correspond to the phase transitions occurring during

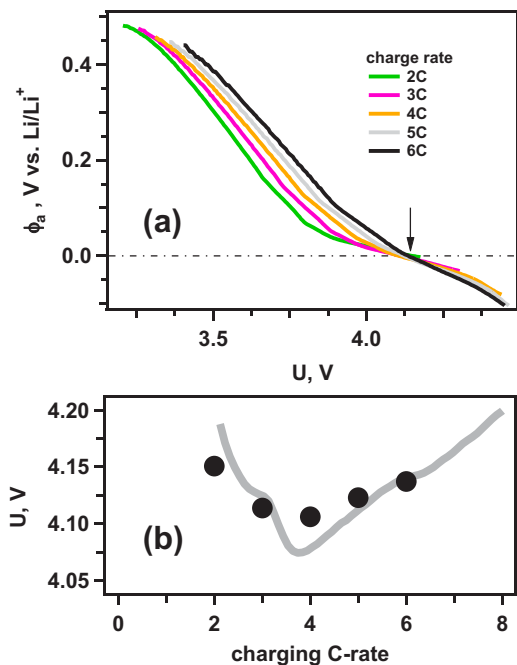


Figure 4. (a) A parametric plot of the anode potential vs. cell voltage at different charge C-rates. The arrow indicates zero-crossing when $\phi_a = 0$. (b) Cell potentials at the zero-crossing (filled circles). The gray line was computed using Eq. 4 and data shown in Figure 6 below. These data suggest that the $\phi_a = 0$ condition would not be met provided that the cell voltage is maintained below 4.0 V regardless of the charging rate. This, however, is not generally correct, as the curves change on repeated cycling, as shown later.

Li staging of graphite (see Figure S4 that shows ϕ_a vs. SOC for C/25 cycling of the same cell). In particular, the 0.11 V feature corresponds to stage-II (LiC_{12}) formation, while the 0.2 V feature corresponds to the onset of long-range ordered intercalation (only Li-carbon solid solutions are observed at lower SOC).^{16–18} Whereas parameter r_1 is analogous to resistance, interpretation of parameter r_2 (that quantifies nonlinearity of the potential response) is less straightforward. For

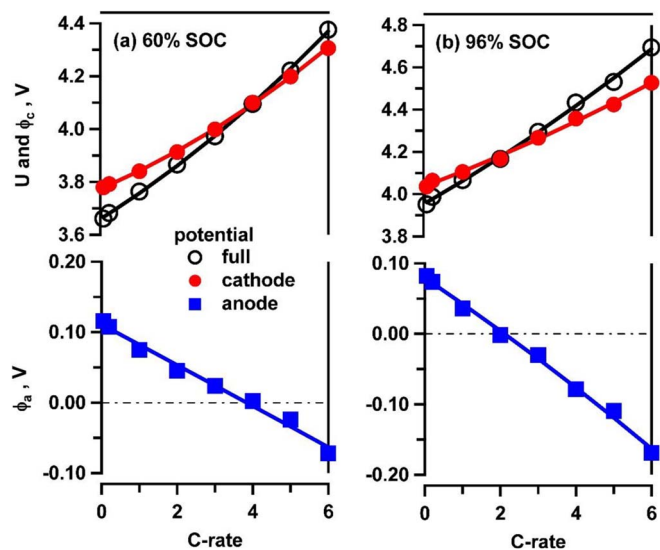


Figure 5. Least squares fits of the cell voltage U and electrode potentials ϕ_c and ϕ_a (in V vs. Li/Li^+) plotted as a function of the C-rate (vertical cross cut in Figure 1). The least squares fits to Eq. 4b are shown with solid lines and measured potentials at fixed q are indicated by symbols. Panels a and b correspond to 60 and 96% charge, with 120 $\text{mAh/g}_{\text{oxide}}$ taken as 100% SOC.

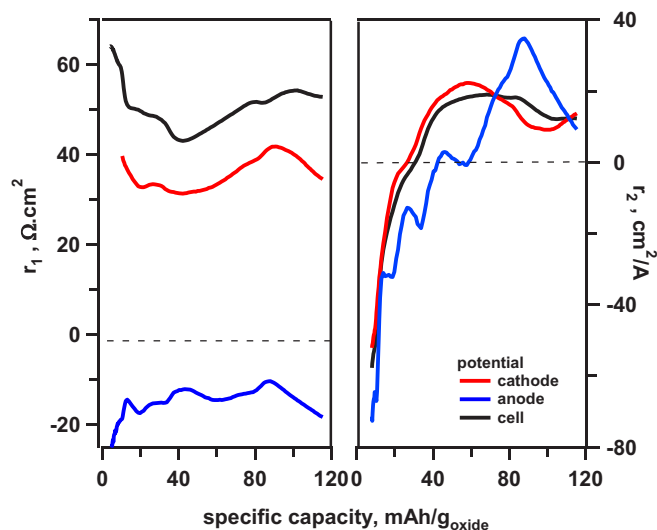


Figure 6. Parameters r_1 (to the left) and r_2 (to the right) obtained by the least-squares fitting of voltage-current curves using Eq. 4 plotted as functions of specific capacity. The potentials are color coded as indicated in the legend. Note that r_2 changes sign for all three potentials.

graphite anode, the dependence of r_2 vs. ϕ_a resembles that for r_1 (see Figure 7b) suggesting that both of these parameters originate from intercalation dynamics (see below). We leave the mechanistic causes for nonlinearity in Eq. 4 an open problem, nevertheless noticing that even the simple treatment in Eqs. 1–3 anticipates the functional form of Eq. 4.

Knowing $r_{1,2}$ allows accurate estimation of all three potentials via Eq. 4, which in turn permits solving the inverse problems (that is, finding q for a given $V(q, I)$) and calculating dependencies between different potentials of interest. This possibility is illustrated in Figure 8 where we used Eq. 4 to calculate capacity and ϕ_a for different fixed voltages U and also to compute $\phi_a = 0$ crossing voltage in Figure 4. As seen from these plots, Eq. 4 cannot only be used to interpolate, but also to extrapolate data to high C-rates for which experimental measurements are complicated by concerns about damage to the cell

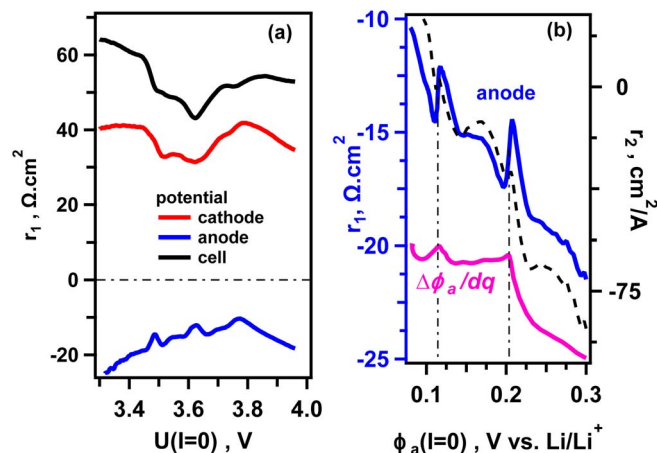


Figure 7. (a) Parameters r_1 from Figure 6 plotted vs. U extrapolated to infinitely small current and (b) the anode $r_{1,2}$ plotted vs. the anode potential, also extrapolated to infinitely small current. The $r_1(U)$ plot in panel (a) has the characteristic “bowl” shape. The $r_{1,2}(\phi_a)$ plots in panel (b) indicate sharp features marked by the vertical arrows. The potentials shown on the horizontal axes were obtained by extrapolation of experimental potentials to zero current using Eq. 4. The $d\phi_a/dq$ curve shown in panel b was obtained by taking numerical derivative of the C/25 charge curve in Figure S4.

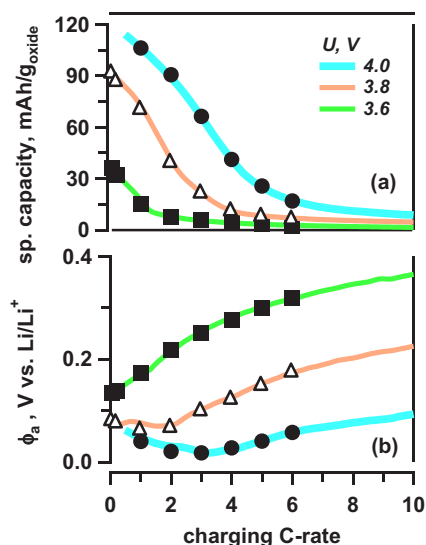


Figure 8. (a) Charge capacity and (b) ϕ_a at $U = 3.6, 3.8$ and 4 V (filled squares, open triangles, and filled circles, respectively) with the solid lines (color coded in panel a) giving the values interpolated and extrapolated using Eq. 4.

materials. This useful property of Eq. 4 results in considerable data reduction.

Pulsed current measurements.—Pulsed current measurements can be used to characterize polarization in a manner distinctly different from using Eq. 4. We remind that one can divide end-of-pulse impedance into the ohmic ($t = 0$) and time-dependent ($t = \tau$) components, as illustrated in Figure S1, to separate fast potential responses (< 0.1 s) from delayed responses (0.1–100 s) that occur due to kinetic processes in the electrodes. Figure 9 shows ASI components at different cell voltages U observed for 3C charge and discharge 30 s long pulses. It is seen that the cathode makes the greater contribution to the impedance at $t = 0$ (Figures 9a, 9b); the impedance is higher at lower cell voltages when the oxide is in a nearly-lithiated state (cf. Figure 6, where the same is observed for r_1). At $t = 0$ the anode impedance has little variation with the voltage or current direction, while the $\Delta\text{ASI}(t = \tau)$ plots show extrema at the potentials corresponding to Li staging plateaus, like the $r_{1,2}$ traces in Figure 7b. The $\Delta\text{ASI}(t = \tau)$ plots for the cathode show undulations that reflect the impedance associated with migration of Li⁺ ions through the lithiated oxide. The magnitude of the ASI as determined from the pulsed-current measurements is lower, yet compares favorably with the r_1 parameter value given in Figure 7.

In Figures 10a and 10b, the anode $\text{ASI}(t = 0)$ and $\Delta\text{ASI}(t = \tau)$ are plotted vs. the anode potential. The variations in these plots can be related to the staging behavior of the graphite and compared to the $r_{1,2}$ behaviors shown in Figure 7b. It is seen that the ohmic component of the impedance (Figure 10a) changes rapidly during the stage I and stage II transitions, and is higher in the single-phase regions (these are shown in Figure 10c using data from Figure S4). In contrast, the anode $\Delta\text{ASI}(t = \tau)$ decreases during the transitions and is lower for the single-phase regions. As show below, this behavior is reproduced in the simulations obtained using the electrochemical model that includes phase transitions in the graphite.

Electrochemical modeling of the pristine cell.—To simulate the observed behaviors before aging occurs, we used an electrochemical model that considers the cathode as a solid solution and uses the Avrami equations to take into account phase transitions between LiC₆, LiC₁₂, and dilute Li-C phases in lithiated graphite.¹² The most important parameters of this model are summarized in Section S1 of the Supporting Information. Below we briefly consider the main results obtained from using this model. For this survey, we adjusted model pa-

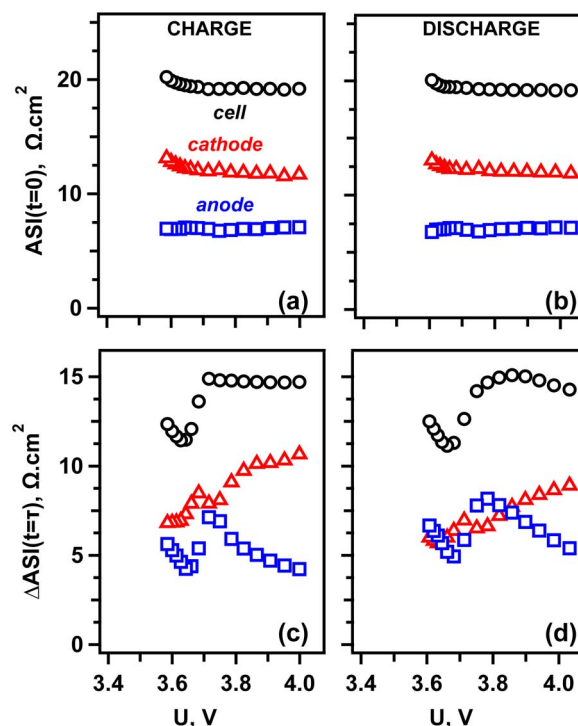


Figure 9. Area specific impedance measurements before the fast charge tests: the ohmic $\text{ASI}(t = 0)$ (a,b) and time-dependent $\Delta\text{ASI}(t = \tau)$ (c,d) for charge (a,c) and 3C discharge (b,d) using 3C, $\tau = 30$ s pulses. Shown in the plot are the full cell, cathode and anode ASI (open circles, triangles, and squares, respectively) plotted as a function of the cell voltage.

rameters to reproduce low-rate behaviors; no further adjustments were made, as we are mainly interested in qualitative effects. Importantly, Li plating was not included into this model.

By conducting computation experiments in the same fashion as the experiments, we found that the model qualitatively reproduced many of the observed behaviors. Most importantly, it correctly gives non-linear dependence of the potentials on the current given by Eq. 4b, so $r_{1,2}$ analysis of computed traces can be carried out in the same way as in the experiment (see Figure 11, which can be compared with Figure 6). The computed r_1 parameters are close but not identical to the computed pulsed-current impedances plotted in Figure S5 (which is consistent with our experiments). Furthermore, the model qualitatively reproduces $r_2(q)$ dependencies for the full-cell and electrode potentials (Figures 6 and 11); in particular, it shows r_2 changing from negative to positive with the increased charge. For the anode potential, the model reproduces Z-like dependences of the anode r_1 and ASI vs. the anode potential (Figures 10 and S6). All in all, our model, which was originally developed to describe a cell operating in low-rate Li insertion regimes, describes (albeit qualitatively) many of the behaviors peculiar to the fast-charging regimes without any additional processes taken into account.

Aging of the cell.—For cycle-life aging experiments, the cell was exposed to eight C-rate escalation laps with HPPC measurements conducted between these laps. To avoid excessive damage, the charge was limited to 42% SOC, so the maximum voltage attained during the test was 4.22 V. Over the duration of the test, the terminal voltage attained at 6C increased by ~ 0.3 V from its original value (Figure 12a). The most dramatic change is seen in the anode potential shown in Figure 12b. The anode potential progressively decreases with each lap; alarmingly, as the cell ages, attaining zero vs. Li/Li⁺ requires increasingly lower charge. Figure 13a shows the zero-crossing capacities and Figure 13b shows terminal anode potentials plotted vs. the C-rate for different laps. The anode potential dependencies become more curved,

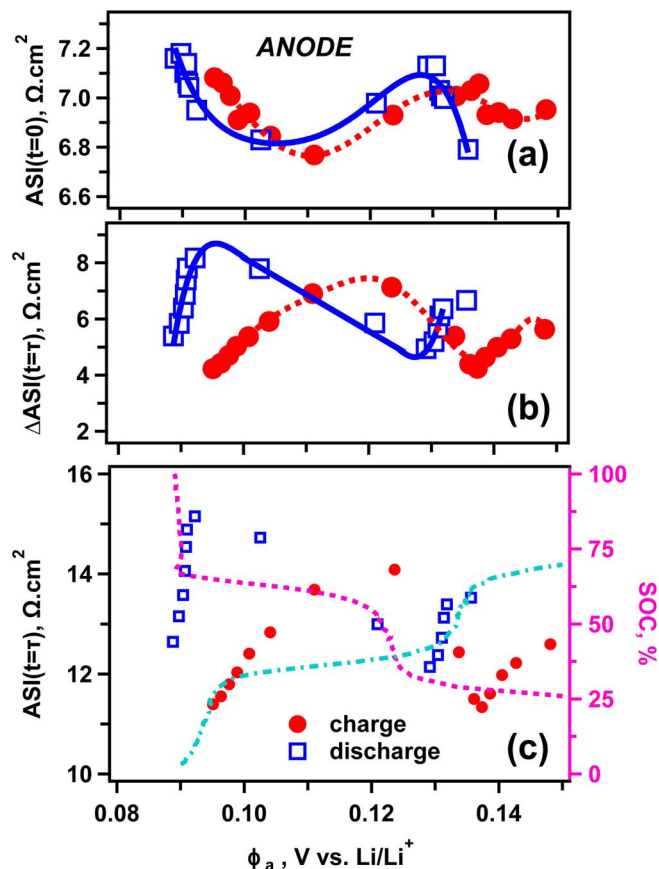


Figure 10. (a,b) Charge (filled circles) and discharge (open squares) contributions to anode ASI from Figures 9c and 9d plotted vs. the anode potential. The curves drawn through the symbols are guides to the eye. In panel c, charge and discharge end-of-pulse anode ASI is juxtaposed on the charge (magenta dashed line) and discharge (cyan dash-dot line) capacity vs. anode potential plots for a C/25 cycle (to the right).

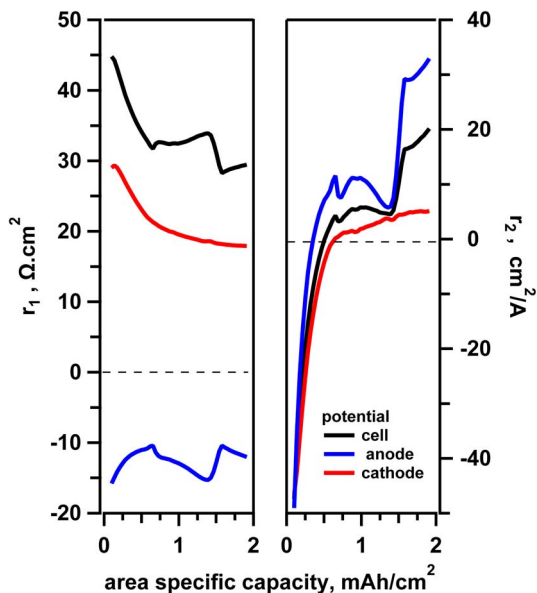


Figure 11. (a) Calculated anode $r_{1,2}$ plotted vs. the area specific capacity. This plot can be compared with Figure 6.

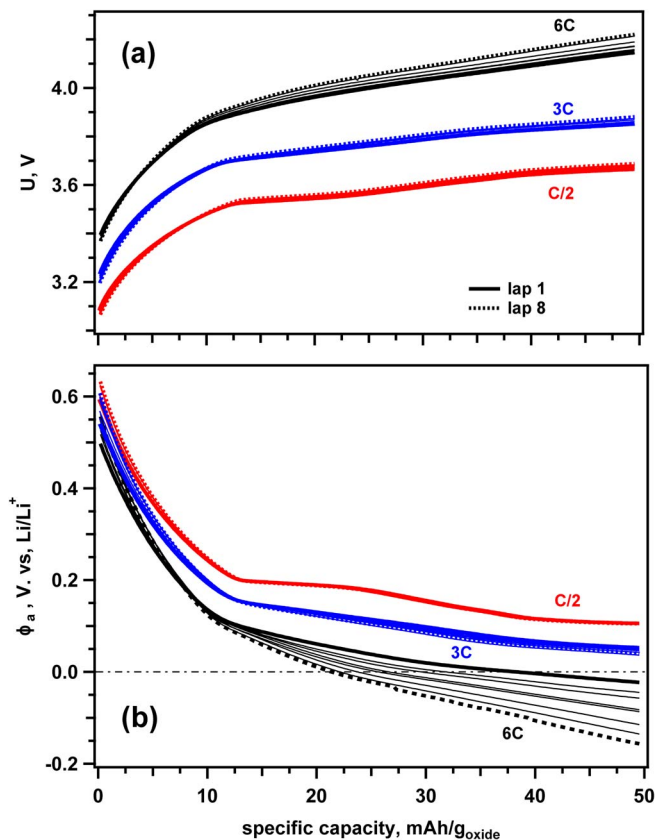


Figure 12. Capacity-limited charging to $50 \text{ mAh/g}_{\text{oxide}}$ (42% SOC). Shown in this plot is the effect of aging on the (a) cell voltage and (b) anode potential during a series of eight escalation laps (with the C-rate progressively increasing from C/2 to 6C and C/5 discharge). The traces are shown for the three current rates indicated in the plot. Lap 1 is shown with the bold solid lines, lap 8 is shown with the bold dashed lines, and the laps in between are shown with thin lines filling the gaps between the first and the last lap in this test.

increasingly deviating from a straight line shown in Figure 3b. At the same time, the initial $d\phi_a/dI$ does not change, implying constancy of the anode impedance. That is also suggested by Figure 13c, where we plot end-of-pulse ASI at different points during the experiment. While for the cathode there is impedance rise, there is almost no change in the anode ASI.

This constancy may not be apparent at a first glance (see Figure S7a) due to gradual slippage of the electrode potentials in aged cells.¹⁹⁻²¹ Due to this slippage, at certain voltages, the anode ASI measured at a fixed voltage can be different in the pristine and aged electrodes. Plotting the same quantities vs. the anode potential (as done in Figure S7b) indicates that when this slippage is taken into account, there is no measurable change in the anode impedance. Thus, not only is there negligible change in the total anode ASI as suggested by Figure 13c: there is, actually, no change both in the ohmic part and in the time-dependent part of the anode ASI. The paradox of Figure 13c is that strong anode polarization occurs without any change in the anode impedance. This includes the conditions at which Li plating certainly occurred in the cell.

It was this unexpected behavior that prompted us to consider alternative ways of quantifying potential response to the constant current, exemplified in the $r_{1,2}$ analysis. As the linear r_1 component is analogous to impedance, it is not surprising to see (Figures 14a and 14b) that this parameter changes little as the cell ages, in agreement with other lines of evidence. For the cathode, the nonlinear component (characterized by r_2) changed some more (Figure S8 shows such curves for the cell voltage), but the greatest change was observed for the anode in Figure 14a. At lower voltages, even the sign of curvature changes

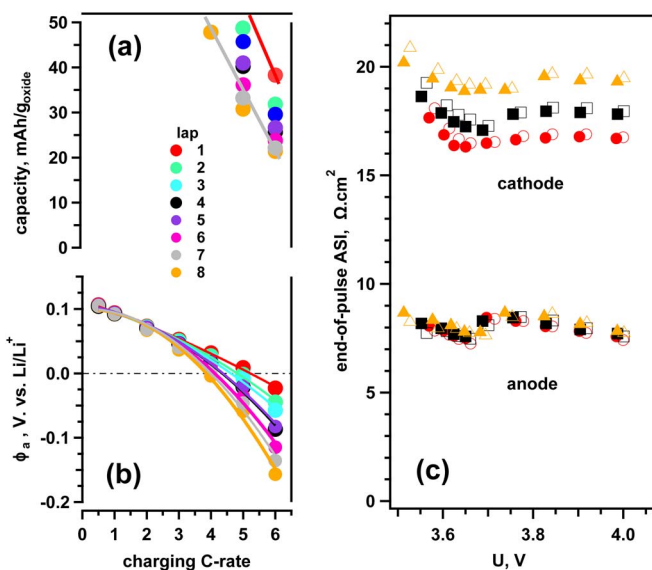


Figure 13. (a) Zero-crossing capacity (at which $\phi_a = 0$ is attained) and (b) anode potential ϕ_a at 50 mAh/g_{oxide} plotted vs. the C-rate for eight successive laps. The straight lines in panel (a) are guides to the eye. As the cell ages, Li plating condition occurs at increasingly lower charge rates (with the “triangular” regions in the upper right corner designating unsafe conditions, while the anode potentials increasingly deviate from the straight line showing the characteristic curvature for high C-rates. Note that the initial slope at low C-rates does not change. (c) End-of-pulse charge (filled symbols) and discharge (open symbols) cathode and anode area specific impedances (3C, 10 s pulses) plotted vs. cell voltage before the test (lap 0, circles), after 4 laps (squares) and after 8 laps (triangles). While there is an increase in the cathode impedance, which is also observed at slow-rate aging of the cathode, there is almost no change in the anode impedance.

as the cell ages, and at high voltages r_2 changed by a factor of 2–3. We conclude that most of the change in the cell polarization incurred by aging is nonlinear and on principle cannot be rationalized in terms of impedance that characterizes a linear part of this response. As far as we know, this kind of change occurs only during fast charging of the cells and has not been reported in the literature.

Note that this nonlinearity only partially resolves the paradox mentioned above: even if the potential response is nonlinear (as strongly suggested by Figure 14a), it should still be observed in our pulsed experiments. To evade detection, this nonlinear response should occur on the time scales that are much longer than typical times of HPPC or EIS measurements. The same is suggested by experiments discussed in Part 3,¹⁴ where we studied relaxation behavior after an abrupt termination of the current. In addition to a current-independent fast-response component, there was also a slow, dispersive component on the time scale of 10^2 – 10^4 s with the rate constants proportional to the C-rate before the current termination. If such a slow, current-dependent response also occurs during charging of the cell, it would qualitatively account for our observations: the constancy of the fast, linear response, the nonlinearity of this response, and the paradox of the systematically increasing anode polarization without the concomitant change in the anode impedance.

Another important consideration is whether the changes in the anode potential shown in Figure 12 originate through Li plating that inevitably occurs when these potentials become strongly negative. In the experiments considered elsewhere, we used our RE to control charging so that the anode potential stayed above +5 mV vs. Li/Li⁺ at any point during aging of the cell. Even in these experiments, the anode potential attained the cutoff condition at lower charge capacities during cell aging, so it seems highly unlikely that this behavior is caused by Li plating *per se*. The same applies to the data shown in Figure 9: even though Li plating certainly occurred under the conditions of our

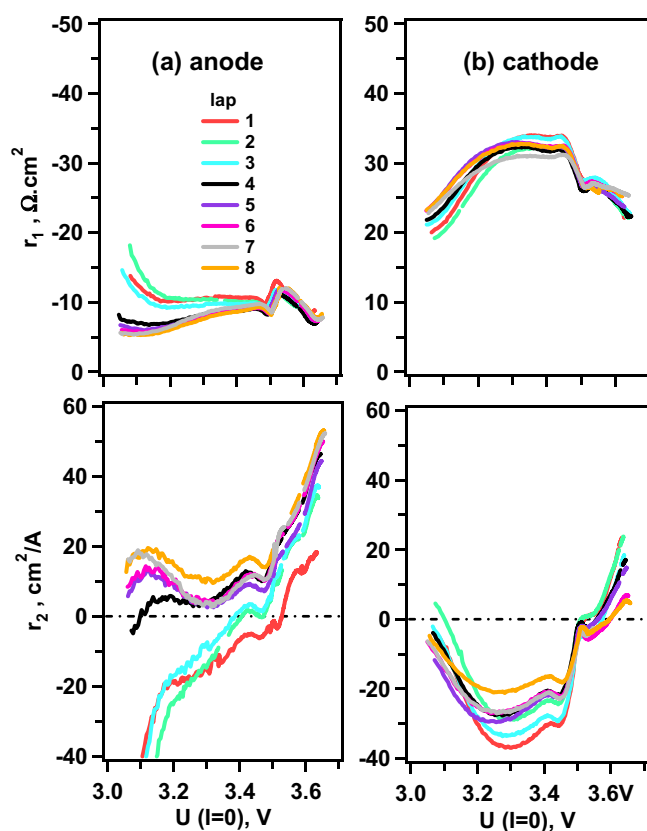


Figure 14. $r_{1,2}$ analysis of aging cells (capacity limited charging between C/2 and 6C to 50 mAh/g) for (a) graphite anode and (b) oxide cathode. Consistently with other lines of evidence, r_1 for both electrodes (the upper two panels) shows little variation as the cell ages. In contrast, r_2 varies significantly, especially for the anode.

experiment (as is also suggested by post mortem examination of disassembled cells), it had no measurable effect on the anode impedance.^{1,22}

Electrochemical modeling of aging.—Can the surprising behaviors we observed above be reproduced in existing electrochemical models?

As there are many such models, we cannot answer this question in general; nevertheless, such models typically include equations for exchange currents at the electrode surfaces, diffusion equations for migration of lithium in the electrolyte and electrode matrices, and (optionally) transitions between different phases in the graphite electrode.²³ Time lags caused by such processes as the latter change due to aging of the cell can potentially explain the observed phenomena.²⁴ The conceptual difficulty with this approach is that such processes need to account for the observed cell polarization without introducing changes in the anode ASI or r_1 . For illustration of this challenge, we selected the model parameter that is potentially capable of “explaining” the anode polarization seen in Figure 12, which is the anode exchange current i_a for lithium insertion into the graphite electrode. For simplicity, we assumed that this rate does not depend on the phase transformations during lithiation.

In Figure 15, the calculated anode potential at 0.84 mAh/cm² (which corresponds to 50 mAh/g_{oxide} in Figures 12–14) is plotted for different C-rates and anode exchange current densities i_a . The computed curves resemble the experimental ones shown in Figure 13b, with the linear $\phi_a(q)$ vs. I dependencies at high i_a and the increasingly curved ones at lower i_a . As in the experimental traces, as i_a decreases, progressively lower charge is required to meet the Li plating condition (compare Figures 13a and S9); i.e., one can interpret aging as systematic lowering of the i_a . Furthermore, the progression of r_2 seen in

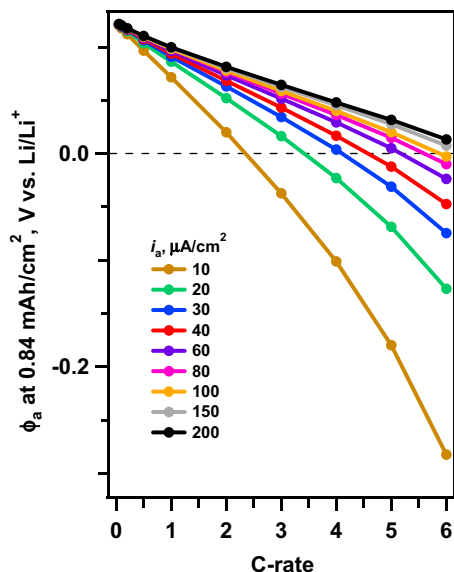


Figure 15. Calculated anode potential at 0.84 mAh/cm² (corresponding to 50 mAh/g_{oxide}) vs. the C-rate for different exchange current densities i_a of Li⁺ insertion into graphite.

Figure 14a (with r_2 becoming increasingly positive at lower capacity) can also be simulated by decreasing i_a , as demonstrated in Figure 16. However, as stated above, a variation in i_a sufficiently great to change the curves shown in Figure 15 would also be expected to change the anode impedance, which is not observed experimentally. This is seen in Figure 17 where the calculated anode r_1 and ASI obtained using 10 s, 3C pulses are plotted together. There is significantly more variation in these calculated parameters over the range of i_a that is required to explain changes in the anode potential (Figure 15) than was observed experimentally. The same was observed when other kinetic parameters in the model, such as Li diffusion coefficients and phase transition rates, were varied: while a slower process could potentially account for the observed changes in the anode potential, it also caused significant

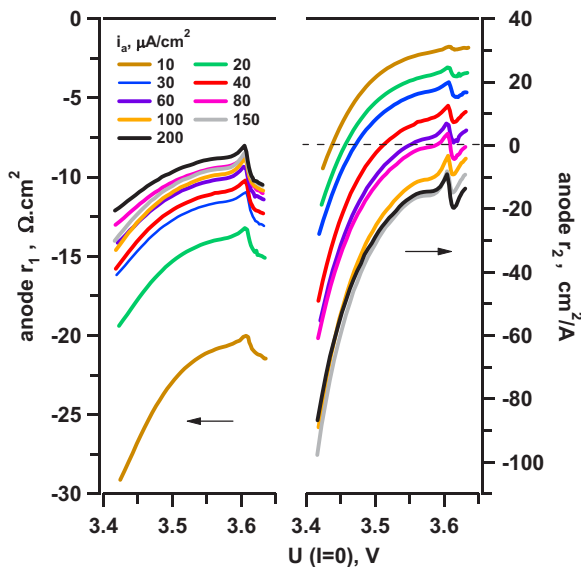


Figure 16. Calculated $r_{1,2}$ plots for the anode potential (different color lines indicate different anode exchange current densities indicated in the upper left corner). The curves correspond to the capacity range between zero and 0.84 mAh/cm². This plot can be compared with the experimental data in Figure 14.

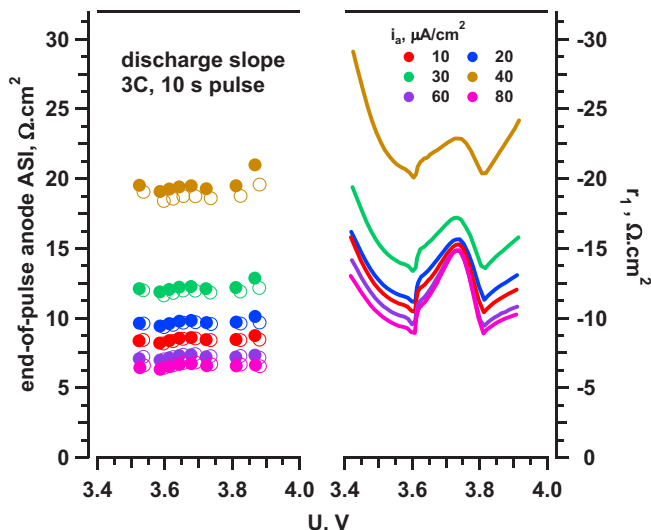


Figure 17. Calculated end-of-pulse area specific anode impedance (on the left; discharge slope, 3C, 10 s pulse; filled symbols are for charge pulses and open symbols for discharge pulses) and r_1 (on the right) plotted vs. the cell voltages. Different colors correspond to different anode exchange current densities indicated in the upper right corner of the plot.

changes in the anode ASI that were not observed. No rate-limiting process considered in our model provided a “natural” explanation for the changes seen in Figures 12b and 13b without introducing excessive variation in the anode ASI.

The main deficiency of our model (and, by extension, all like models) is that it yields only fast response ($< 10^2$ s) to a change in the current, whereas several lines of evidence suggest there is also a current-dependent delayed response, which is missing from the model. We plan to include these features in future versions of the model so that the simulations can provide a better fit to the experimental data.

Conclusions

In this study, thin-wire Li/Cu reference electrodes were used for in situ monitoring of the NCM523||graphite cells during fast galvanostatic charging.

Our main result is the surprising generality of Eq. 4 that is derived for small-current perturbations. This equation remains accurate even for high currents, capturing nonlinear effects introduced by these currents. This equation holds equally well for potentials computed using Newman style electrochemical models, which also suggests its generality. The equation can be applied both to the full-cell potential and individual electrode potentials. Consequently, the complexity of potential surfaces can be reduced to two sets of parameters r_1 and r_2 for each electrode, so these surfaces can be easily interpolated and extrapolated using Eq. 4. The r_1 parameters are similar in magnitude and behavior to the area specific impedances (ASI) determined from pulsed-current measurements, whereas r_2 parameters (that characterize nonlinearity of the potential response) cannot be determined from other types of measurement.

While the interpretation of r_2 is not straightforward (as many dynamic processes occur in the cell), calculating this parameter and its q -dependence could be a target for cell modelers. Even though the general behavior of r_1 and r_2 (as well as the ASI determined using pulsed currents) is captured in the electrochemical models, there are certain aspects of behavior that may require a new approach. This primarily refers to the changes observed in the potential-capacity plots observed as the cell ages: whereas the changes are qualitatively consistent with the increasing anode polarization, no change in the anode impedance is observed, suggesting that the polarization originates almost entirely through nonlinear, delayed potential responses. In Part 3¹⁴ we revisit

this issue and provide direct evidence for such delayed responses after the currents are turned off. As the potential during galvanostatic charge is a cumulant of all such time responses, the resulting dependence of such potentials on the current becomes complex.

Our study suggests, quite unexpectedly, that the difficulty of modeling fast-charging may be less in the simulation of fast processes, but rather in simulation of slow after-effects of these fast processes, of still unknown nature, that are stretched over many decades in time and provide a major contribution to electrode polarization.

Acknowledgments

I.A.S. and M.-T.F.R. made equal contributions to this manuscript. Support from the U.S. DOE's Office of Vehicle Technologies, specifically from Brian Cunningham and Samm Gillard, is gratefully acknowledged. The electrodes used in this article are from Argonne's Cell Analysis, Modeling and Prototyping (CAMP) Facility, which is supported within the core funding of the Applied Battery Research (ABR) for Transportation Program. We are grateful to colleagues in the XCEL program, especially to Steve Trask and Andy Jansen. The submitted manuscript has been created by UChicago Argonne, LLC, Operator of Argonne National Laboratory ("Argonne"). Argonne, a U.S. Department of Energy Office of Science laboratory, is operated under Contract No. DE-AC02-06CH11357. The U.S. Government retains for itself, and others acting on its behalf, a paid-up nonexclusive, irrevocable worldwide license in said article to reproduce, prepare derivative works, distribute copies to the public, and perform publicly and display publicly, by or on behalf of the Government.

ORCID

Ilya A. Shkrob  <https://orcid.org/0000-0002-8851-8220>

Marco-Tulio Fonseca Rodrigues  <https://orcid.org/0000-0003-0833-6556>

Daniel P. Abraham  <https://orcid.org/0000-0003-0402-9620>

References

1. M.-T.F. Rodrigues, K. Kalaga, S.E. Trask, D.W. Dees, I.A. Shkrob, and D.P. Abraham, *J. Electrochem. Soc.*, **166**, A996 (2019).
2. M. Bauer, M. Wachtler, H. Stowe, J. V. Persson, and M. A. Danzer, *J. Power Sources*, **317**, 93 (2016).
3. E. Hu, X. Wang, X. Yu, and X.-Q. Yang, *Acc. Chem. Res.*, **51**, 290 (2018).
4. X.-G. Yang and C.-Y. Wang, *J. Power Sources*, **402**, 489 (2018).
5. P. Arora, M. Doyle, and R. E. White, *J. Electrochem. Soc.*, **146**, 3543 (1999).
6. C. Mao, R. E. Ruther, J. Li, Z. Du, and I. Belharouak, *Electrochem. Commun.*, **97**, 37 (2018).
7. J. E. Harlow, S. L. Glazier, J. Li, and J. R. Dahn, *J. Electrochem. Soc.*, **165**, A3595 (2018).
8. A. M. Colclasure, A. R. Dunlop, S. E. Trask, B. J. Polzin, A. N. Jansen, and K. Smith, *J. Electrochem. Soc.*, **2019**, A1412 (2019).
9. D. Dees, E. Gunen, D. Abraham, A. Jansen, and J. Prakash, *J. Electrochem. Soc.*, **152**, A1409 (2005).
10. D. Dees, E. Gunen, D. Abraham, A. Jansen, and J. Prakash, *J. Electrochem. Soc.*, **155**, A603 (2008).
11. D. P. Abraham, M. M. Furczon, S. H. Kang, D. W. Dees, and A. N. Jansen, *J. Power Sources*, **180**, 612 (2008).
12. K. G. Gallagher, D. W. Dees, A. N. Jansen, D. P. Abraham, and S.-H. Kang, *J. Electrochem. Soc.*, **159**, A2029 (2012).
13. M. D. Murbach, V. W. Hu, and D. T. Schwartz, *J. Electrochem. Soc.*, **165**, A2758 (2018).
14. Ilya A. Shkrob, M.-T. F. Rodrigues, and D. P. Abraham, *J. Electrochem. Soc.*, (2019), submitted.
15. M. Klett, J. A. Gilbert, S. E. Trask, B. J. Polzin, A. N. Jansen, D. W. Dees, and D. P. Abraham, *J. Electrochem. Soc.*, **163**, A875 (2016).
16. K. P. C. Yao, J. S. Okasinski, K. Kalaga, I. A. Shkrob, and D. P. Abraham, *Energy Environ. Sci.*, **12**, 656 (2019).
17. A. Missyul, I. Bolshakov, and R. Shpanchenko, *Power Diffraction*, **32**, S56 (2017).
18. T. Ohzuku, Y. Iwakoshi, and K. Sawai, *J. Electrochem. Soc.*, **140**, 2490 (1993).
19. M. Klett, J. A. Gilbert, K. Z. Pupek, Stephen E. Trask, and D. P. Abraham, *J. Electrochem. Soc.*, **164**, A6095 (2017).
20. J. A. Gilbert, I. A. Shkrob, and D. P. Abraham, *J. Electrochem. Soc.*, **164**, A389 (2017).
21. J. A. Gilbert, J. Bareño, T. Spila, S. E. Trask, D. J. Miller, B. J. Polzin, A. N. Jansen, and D. P. Abraham, *J. Electrochem. Soc.*, **164**, A6054 (2017).
22. T. R. Tanim, E. J. Dufek, M. Evans, C. Dickerson, A. N. Jansen, B. J. Polzin, A. R. Dunlop, S. E. Trask, R. Jackman, I. Bloom, Z. Yang, and E. Lee, *J. Electrochem. Soc.*, **166**, A1926 (2019).
23. A. M. Colclasure, A. R. Dunlop, S. E. Trask, B. J. Polzin, A. N. Jansen, and K. Smith, *J. Electrochem. Soc.*, A1412 (2019).
24. F. Jiang and P. Peng, *Sci. Reports*, **6**, 32639 (2016).